

1 **Constructing physical-based rainfall landslides prediction model:**  
2 **Insights from rainfall threshold curves database of slope units**

3 Kai Wang<sup>1\*</sup>, Linmao Xie<sup>1</sup>, Shuailong Xie<sup>1</sup>, Shaojie Zhang<sup>2\*</sup>, Yongyang Jiang<sup>3</sup>, Ji Zhang<sup>4</sup>, Lin Zhu<sup>1</sup>, Zhiliu Wang<sup>1</sup>,  
4 Fuzhou Qi<sup>1</sup>

5 *1. School of architecture and civil engineering, Zhongyuan University of Technology, Zhengzhou, 450007, China*

6 *2. Key Laboratory of Mountain Hazards and Earth Surface Process, Institute of Mountain Hazards and Environment,*  
7 *Chinese Academy of Sciences, Chengdu, 610041, China*

8 *3. Zhejiang Zhongnan Construction Group Steel Structure Co., Ltd, Hangzhou, 311400, China*

9 *4. Sichuan Institution of Geological Engineering Investigation Group Co.LTD, Chengdu, 610041, China*

10 **Abstract:** The commonly used rainfall threshold warning method relies heavily on historical  
11 rainfall and landslide inventory data, which limits its applicability in regions that lack these data.  
12 While physical methods do not rely on landslide inventories to establish warning criteria, the  
13 calculation of the safety factor typically requires considerable time. To address these issues, this  
14 study integrates physical methods, rainfall threshold warning methods, and slope units to develop a  
15 rapid forecasting model for rainfall landslides at a regional scale. A hydrological analysis technique  
16 for slope units based on grid cells was developed to calculate the instability probability of slope  
17 units. Then, each slope unit was analyzed under 20 levels of antecedent effective precipitation and  
18 nearly 200 combinations of rainfall intensity (I) and duration (D) to derive the key fitting parameters  
19  $\alpha$  and  $\beta$  of the I-D curves under various rainfall scenarios. The application results from Fengjie  
20 County indicate that the model runs in less than 12 min, with missing alarm and false alarm rates of  
21 11.8% and 21.1%, respectively, highlighting its excellent potential for practical application. This  
22 study is expected to provide insights for the rapid forecasting of rainfall landslides in the  
23 impoverished mountainous regions of developing countries.

24

25

26 **Key words:** Landslide forecasting model, Slope unit, Fitting parameters, Warning database

27

28

29

30

31

32

33

---

\* Corresponding Authors 1: Kai Wang

E-mail: [6696@zut.edu.cn](mailto:6696@zut.edu.cn)

\* Corresponding Authors 2: Shaojie Zhang

E-mail: [sj-zhang@imde.ac.cn](mailto:sj-zhang@imde.ac.cn)

1 **1 Introduction**

2 Rainfall-induced landslides at a regional scale are among the most common types of natural  
3 hazards worldwide. Reports indicate that in the United States, rainfall-triggered landslides and  
4 secondary hazards result in 25–50 fatalities and economic losses of approximately \$2 billion  
5 annually (He et al., 2016). This loss is even more severe in developing countries in the Third World  
6 (Wang et al., 2024; Wang et al., 2021; Wang et al., 2023). In recent years, numerous studies have  
7 indicated that regional landslide forecasting is highly effective for hazard prevention and mitigation.  
8 Researchers have developed various rainfall landslide forecasting models based on statistical and  
9 physical methods (Aristizábal et al., 2016; Baum et al., 2008; Bezak et al., 2016; Bogaard et al.,  
10 2018; Cuomo et al., 2021; Liang et al., 2021; Medina et al., 2021; Pinho et al., 2022; Tufano et al.,  
11 2021; Wang et al., 2013; Zhang et al., 2021; Zhang et al., 2019; Moeineddin et al., 2023; Li et  
12 al.,2025).However, there are still several unresolved issues in regional landslide forecasting, making  
13 accurate and efficient warnings a significant global challenge.

14 The first major issue is the selection of forecasting methods. The presented statistical  
15 approaches generally depend on historical precipitation and landslide inventory data to construct  
16 the rainfall threshold curves. Recently, researchers proposed different types of rainfall threshold  
17 curves, including Intensity-Duration(I-D), Rainfall event-Duration (E-D), Rainfall event-Intensity,  
18 (E-I), Intraday rainfall and antecedent effective rainfall (IR-AER), Intensity-Probability (I-P), and  
19 Intensity-Duration-Mean areal rainfall( I-D-MEAR)(Brunetti et al., 2010; Hong et al., 2005; Rosi  
20 et al., 2020; Zhuang et al., 2014). The I-D curve is the most extensively used among these types.  
21 The I-D curve is typically fitted in either Cartesian coordinates or a double-logarithmic coordinate  
22 system, and the equation of the curve is governed by two key fitting parameters,  $\alpha$  and  $\beta$ , expressed  
23 as follows:

24 
$$I = \alpha D^\beta \tag{1}$$

25 where  $\alpha$  and  $\beta$  are derived from the statistical analysis of historical rainfall and landslide data.

26 Studies indicate that statistical methods are applicable in regions with abundant historical  
27 records of rainfall landslides because these areas can provide sufficient samples for fitting the I-D  
28 curve(Bezak et al., 2016; Hong et al., 2017; Kanungo et al., 2014; Kim et al., 2020; Ma et al., 2015;  
29 Marra, 2018; Pradhan et al., 2018). However, in the poor mountainous regions of the Third World,  
30 many areas that are severely affected by landslides lack professional monitoring devices and rain

1 gauges, potentially limiting the application of statistical approaches(Zhang et al., 2021; Zhang et al.,  
2 2019). In contrast, physical methods typically rely on hydrological and mechanical analyses to  
3 calculate the safety factors of landslides under different rainfall scenarios, thereby reducing the  
4 reliance on historical rainfall and landslide observation data. In regions where landslide inventory  
5 data are scarce, physical methods could serve as promising alternatives (Zhang et al., 2021; Zhang  
6 et al., 2019). However, physical methods require historical landslide data to validate the accuracy  
7 of the forecasting results, and the safety factor calculation process typically requires a considerable  
8 amount of time. This computational burden increases substantially when considering the stability  
9 analysis of thousands of slopes at the regional scale, making it difficult to ensure the efficiency of  
10 real-time warnings (Zhang et al., 2021).

11 The second issue pertains to the selection of prediction unit. Clearly defined prediction units  
12 enable residents to identify the specific locations where landslides are likely to occur while also  
13 providing guidance for local governments to develop emergency schemes. However, the I-D  
14 warning curves derived from statistical methods can only provide general trends of hazards within  
15 the region but cannot pinpoint the specific locations of landslide occurrences. Grid cells improve  
16 the clarity of the prediction results to some extent, as the specific locations of each grid within the  
17 area are well defined (Zhang et al., 2021). Researchers have employed grid cells to establish multiple  
18 physical forecasting models such as Shallow Landslide Stability model (Montgomery et al., 1994),  
19 Stability Index Mapping (SINMAP) (Tarboton et al., 1970), The Three-dimensional Fully  
20 Distributed Hydrological model-Safety factor(GEOTop-FS)(Rigon et al., 2006), Transient Rainfall  
21 Infiltration and Grid-Based Regional Slope-Stability Analysis(TRIGRS)(Baum et al., 2008), High  
22 Resolution Slope Stability Simulator(HIRESSS) (Rossi et al., 2013), Hillslope-scale Shallow  
23 Landslide Induced Debris Flow Risk Evaluation(H-slider)(Liang et al., 2021), Open and Distributed  
24 Hydrological Simulation and Landslides (SHIA\_Landslide) (Aristizábal et al., 2016), Shallow  
25 Landslides Instability Prediction (SLIP)(Montrasio et al., 2016), and Fast Shallow Landslide  
26 Assessment Model (FSLAM)(Guo et al., 2022). However, the morphology of grid cells does not  
27 accurately characterize the topographical features of natural hillslopes (Domènech et al., 2019;  
28 Zhang et al., 2021), resulting in a lack of clear geomorphological significance. In practical  
29 applications, a natural slope can be segmented into a series of grid cells, in which each grid is  
30 assigned a different alert level. This indicates that a high warning level in a grid cell does not mean

1 that the entire slope will experience a slide.

2 In contrast, slope units can represent the topographical features of landslides more accurately,  
3 and their boundaries are easily discernible in field environments. Currently, there are various  
4 methods for extracting slope units, including the DEM-based hydrological process analysis  
5 method(Turel et al., 2011), r.slopeunits method(Alvioli et al., 2020), curvature watershed  
6 methods(Yan et al., 2021), MIA-HSU methods(Wang et al., 2019), and multi-scale image  
7 segmentation methods (Huang et al., 2021). In recent years, researchers have developed forecasting  
8 models utilizing slope units, validating their promising application potential in predicting rainfall-  
9 induced landslides (Wang et al., 2023; Zhang et al., 2021).

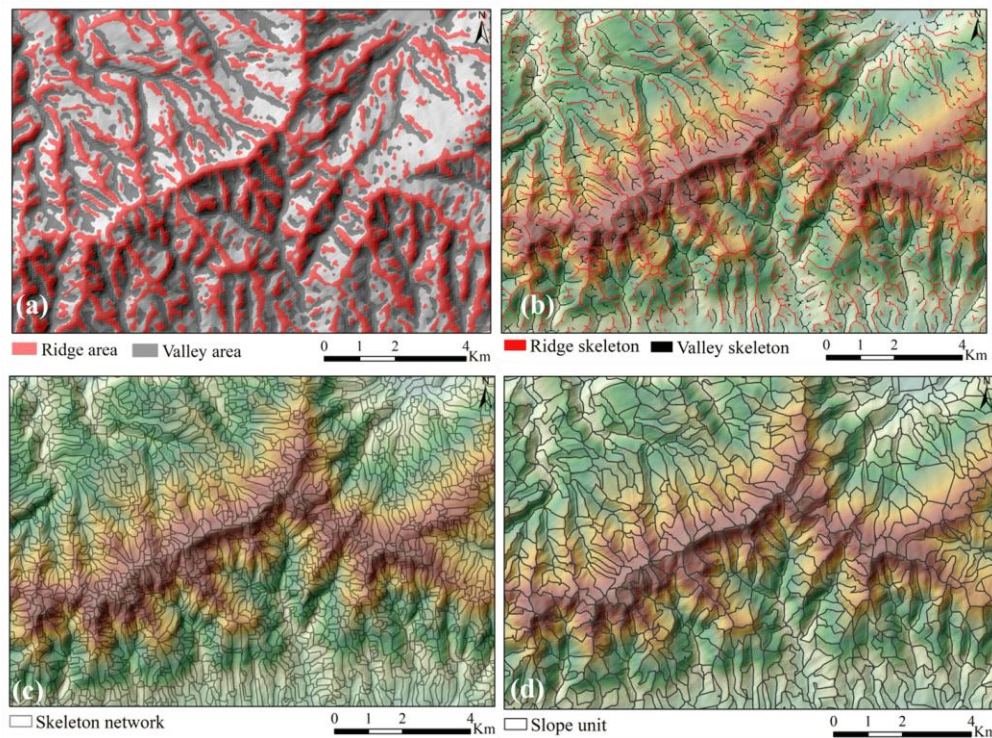
10 Addressing the issues outlined in regional landslide forecasting, this study focuses on the  
11 integration of slope units, physical methods, and rainfall parameterized warning techniques to  
12 develop a rapid forecasting model applicable to large areas on a scale of thousands of square  
13 kilometers. Within this model, we no longer pay attention to the positional relationship between the  
14 rainfall data of a landslide and the I-D curve, but concentrate on the key fitting parameters  $\alpha$  and  $\beta$   
15 of the I-D curve for each slope unit. To facilitate this, we developed a rainfall infiltration simulation  
16 technique rooted in grid cells within slope units and subsequently utilized physical methods to  
17 analyze the instability probability for slope units under different rainfall scenarios. For each slope  
18 unit, we designed rainfall scenarios comprising various antecedent rainfall levels combined with  
19 hundreds of rainfall intensity and duration combinations. This allowed us to obtain the key  
20 parameters  $\alpha$  and  $\beta$  of the I-D curves for different rainfall scenarios, thereby constructing a database  
21 of parameters  $\alpha$  and  $\beta$  under various antecedent precipitation levels. A case study in Fengjie County,  
22 in the Three Gorges Reservoir area, was conducted to validate the reliability of the proposed method.  
23 This research is expected to provide valuable insights for regional landslide forecasting in  
24 impoverished mountainous areas in the developing world.

## 25 **2 Methodology**

### 26 **2.1 The slope unit extraction method MIA-HSU**

27 In this study, we employed the MIA-HSU method to extract slope units(Wang et al., 2021;  
28 Wang et al., 2019; Wang et al., 2023). In the MIA-HSU method, each HSU(homogeneous slope unit)  
29 is defined as a continuous and homogeneous geomorphological entity. This definition implies that  
30 terrain features related to slope and aspect are uniform within each HSU, with boundaries indicating

1 transitions in topographical features. The MIA-HSU method consists of two steps. The first step  
 2 involves partitioning the Digital Elevation Model (DEM) into small regions with homogeneous  
 3 terrain characteristics. In this step, the MIA-HSU method utilizes terrain curvature analysis to  
 4 identify ridge and valley regions (Figure 1a) and then extracts the morphological skeleton lines of  
 5 ridge and valley areas to characterize topographic relief. Morphological algorithms (such as dilation  
 6 and erosion) were used to extract the morphological skeletons of ridges, valleys, and flat areas from  
 7 the DEM (Figure 1b), ultimately connecting these skeletons into a closed network (Figure 1c). Thus,  
 8 each small region within the network exhibits uniform geomorphological characteristics. The  
 9 second step involves merging small adjacent regions. The MIA-HSU method employs the principal  
 10 component analysis (PCA) method to derive fitted planes from localized terrain regions, followed  
 11 by the implementation of vector similarity criteria to merge adjacent small regions, thereby  
 12 generating HSUs(Figure 1d).



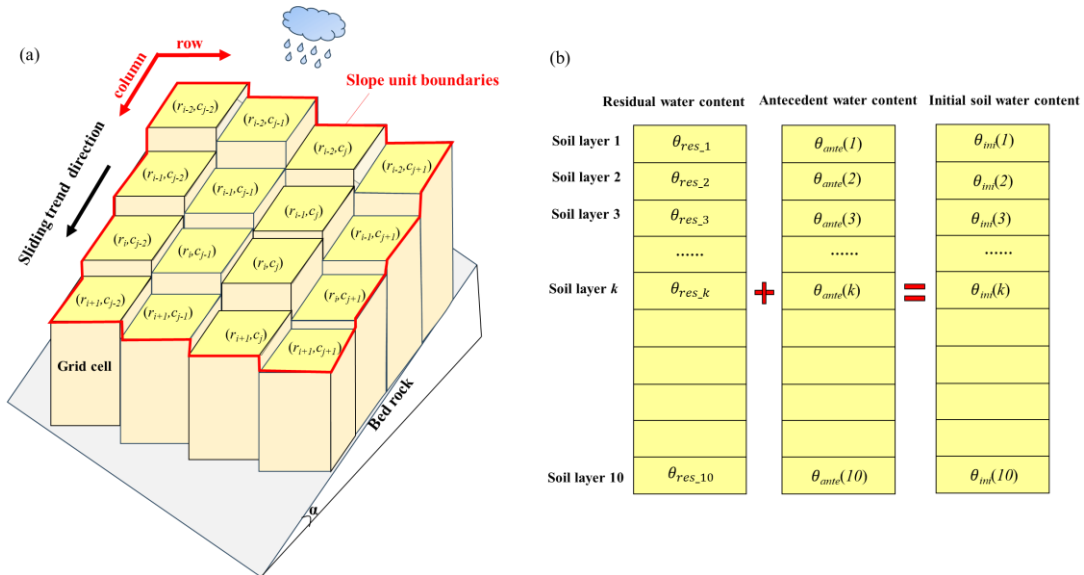
13  
 14 Figure 1 HSU extraction process: a. the identification of ridge and valley areas; b. the morphological skeleton line  
 15 extraction for ridge and valley areas; c. the morphological skeleton closed network; d. HSU extraction result

## 16 2.2 The HSU hydrologic simulation technique based on grid cells

### 17 (1) The identification for row and column information of grid cell within HSUs

18 From a geometric perspective, an HSU can be regarded as a spatial polygon that signifies a  
 19 landform entity with homogeneous terrain features in the field environment. At the regional scale,  
 20 there is obvious heterogeneity in the topography and boundary characteristics among different

1 HSUs(Wang et al., 2021; Wang et al., 2019; Wang et al., 2023), resulting in the immaturity of  
 2 hydrological analysis methods based on slope units. In contrast, hydrological analysis methods  
 3 based on grid cells are well-developed. Some researchers have employed grid cells integrated with  
 4 an infinite slope model or the limit equilibrium method to conduct regional landslide assessment or  
 5 prediction(Gu et al., 2014; Wang et al., 2023; Zhang et al., 2021; Zhuang et al., 2016). In this study,  
 6 each HSU was conceptualized as a composition of grid cells with similar microtopographic features,  
 7 as illustrated in Figure 2a. For each HSU, we utilized GIS spatial analysis tools to quantify the  
 8 number of grid cells contained within it and their corresponding row and column positional  
 9 information, thus establishing a comprehensive database that includes the position information of  
 10 the grid cells within each HSU.



11  
 12 Figure 2 The diagram for HSU-grid cell hydrological connection: a. Grid cells contained within HSU ( $r_i, c_j$  represent  
 13 the row and column of grid cells contained within HSU, respectively)

14 **(2) Initial water content assignment of HSUs**

15 After obtaining the grid cell information contained within each HSU, conducting a rainfall  
 16 infiltration analysis for these grid cells represents a complex and important task. One issue that  
 17 cannot be overlooked is initial moisture content. For landslides in the Three Gorges Reservoir area  
 18 of China, the soil typically experiences a prolonged dry winter before the rainy season (May to  
 19 September). Previous research indicates that the residual moisture content of slopes before the rainy  
 20 season averages approximately 7% to 8% (Wang et al., 2023). Accordingly, this study categorizes  
 21 the initial water content into two components: the residual moisture content ( $\theta_{res}$ ) and the moisture  
 22 content increment caused by antecedent precipitation( $\theta_{ante}$ ). Here,  $\theta_{res}$  reflects the average moisture

1 level of the soil prior to the rainy season, while  $\theta_{ante}$  indicate the increase in moisture content due to  
 2 antecedent effective precipitation prior to landslide occurrence.

3 In this study, each grid cell is stratified into ten soil layers, each with a thickness of 0.2 m  
 4 (Figure 2b). For the Three Gorges Reservoir area, the regional landslides triggered by rainfall were  
 5 mainly shallow (with thicknesses of 2-3 m). Therefore, variations in residual moisture content  
 6 within the soil depth were disregarded, and the same residual moisture content value was assigned  
 7 to each soil layer. Following this, we applied steady-state infiltration theory to simulate the  
 8 distribution of moisture content across the soil layers influenced by antecedent precipitation, thereby  
 9 allocating the antecedent rainfall to each soil layer. The calculation for  $\theta_{ini}$  of each soil layer within  
 10 the grid cell is as follows:

$$\theta_{ini}(k) = \theta_{ante}(k) + \theta_{res} \quad (k=1,2,3 \dots n) \quad (2)$$

11 Where  $n$  represents the number of soil layers, and here  $n = 10$ ;  $\theta_{ini}(k)$  indicates the initial  
 12 moisture content of each soil layer;  $\theta_{ante}(k)$  refers to the moisture change in each soil layer due to  
 13 previous precipitation;  $\theta_{res}$  stands for the residual moisture content in the grid cell.

### 15 (3) Rainfall infiltration process simulation of grid cell

16 After obtaining the initial moisture content distribution, the 1-dimensional Richards infiltration  
 17 equation was used to solve the moisture content distribution in the grid cell during the rainfall  
 18 infiltration process.

$$\frac{\partial \theta}{\partial t} = \frac{\partial}{\partial z} \left[ D(\theta) \cdot \frac{\partial \theta}{\partial z} \right] - \frac{\partial K(\theta)}{\partial z} \quad (3)$$

19 Where  $D(\theta)$  represents the value of soil water diffusivity under unsaturated conditions and has

$$21 D(\theta) = K(\theta) / \frac{d\theta}{d\psi_m} .$$

22 The finite difference scheme outlined above was formulated for numerical simulation of  
 23 hydrological processes. The lower boundary, identified as impermeable, is based on the maximum  
 24 soil depth of the grid cell. The upper boundary of each grid cell was designated as an infiltration  
 25 boundary. When the rainfall intensity  $I(t)$  is less than the infiltration capacity of the topsoil, all  
 26 precipitation infiltrates into the soil, and no runoff is generated. In this scenario, the infiltration  
 27 boundary of precipitation was governed by the following differential equation:

$$28 -D(\theta) \frac{\partial \theta}{\partial z} + K(\theta) = I(t) \quad (4)$$

29 When the rainfall intensity exceeded the soil infiltration capacity, the excess portion was

1 transformed into overland flow. At this point, the rainfall infiltration boundary was governed by the  
2 following equation:

$$3 \quad \theta = \theta_s \quad (5)$$

4 Where  $\theta_s$  is the saturated water content of the grid cell.

#### 5 (4) Soil water content generation of HSU

6 Following the calculation of the soil moisture for individual grid cells, the soil water  
7 distribution of the HSU was computed as follows:

$$8 \quad \theta_{HSU}(k) = \frac{\sum_{k=1}^n \theta(k)}{n} \quad (6)$$

9 where  $\theta_{HSU}(k)$  represents the moisture content of the  $k$ th layer of the HSU,  $\theta(k)$  denotes the  
10 moisture content of the  $k$ th layer in the grid cell.  $n$  is the number of soil layers ( $n = 10$ ).

### 11 2.3 $HSU_{prob}$ : the calculation of instability probability of HSUs

#### 12 (1) Profile extraction

13 After calculating the soil water content within each HSU, analyzing the stability of HSUs  
14 during the rainfall infiltration process is another important task. At present, the time required to  
15 carry out 3D analysis for each HSU on a large regional scale is too large, so extracting the calculation  
16 profile of the HSU becomes a reasonable selection. Currently, there is no uniform method for  
17 extracting the calculation profile of HSUs. Some reasonable assumptions are summarized as follows:  
18 the position of the profile line should reflect the elevation difference between the front and back  
19 edges of the slope, and the centroid point of the HSUs should be on the calculated profile to ensure  
20 that the soil weight on both sides of the calculated section is relatively uniform, and the areas of the  
21 two sections should be close to each other.

22 Based on these considerations, we developed a fast extraction algorithm HSU-profile (Wang et  
23 al., 2021; Wang et al., 2023) for HSU profiles at large regional scales, which can be divided into  
24 three steps:

25 First, the highest elevation point  $H$  of the HSU polygon is connected to centroid point  $C$  to  
26 obtain line segment  $L_1$ , which intersects the HSU polygon at point  $J_1$  (Figure 3b). Line segment  $L_1$   
27 divides the HSU polygon into two parts, and the areas of the two parts,  $S_1$  and  $S_2$  are calculated to  
28 obtain the area ratio  $A = S_1 / S_2$ .

29 Next, the lowest elevation point  $L$  and centroid  $C$  are connected to form line segment  $L_2$ , as

1 shown in Figure 3 b. Determine the intersection point  $J_2$  between  $L_2$  and the polygon of the slope  
 2 unit is determined. At this point, the HSU was divided into two parts by line segment  $L_2$ , and the  
 3 areas of the two parts,  $S_3$  and  $S_4$ , were calculated to obtain the area ratio  $B=S_3/S_4$ .

4 Finally,  $|A|$  and  $|B|$  are compared. A smaller absolute value of A indicates that line segment  $L_1$   
 5 divides the areas on both sides of the HSU polygon more evenly. In this case,  $L_1$  is selected as the  
 6 profile line. Otherwise, the line segment  $L_2$  was chosen as the profile line.

7 (2) Calculation of safety factor  $F_s$  calculation

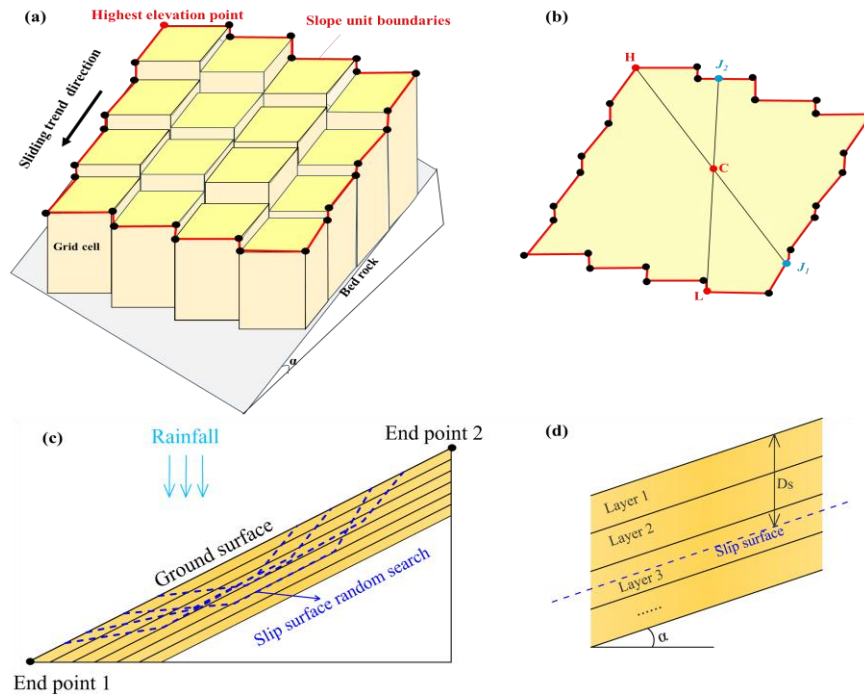
8 For each HSU, the Monte Carlo method was used to generate a large number of potential  
 9 polyline-type slip surfaces (Figure 3c), and the random walk method(Greco, 1996; Zhang et al.,2006)  
 10 was employed to search for the critical slip surface. The infinite slope model was used to calculate  
 11 the safety factor  $F_s$  of each potential slip surface as follows:

$$12 \quad F_s = \frac{\tan \varphi}{\tan \alpha} + \frac{c + u_s \tan(\varphi^b)}{\gamma_s D_s \cos \alpha \sin \alpha} \quad (7)$$

13 where  $c$  is the effective cohesion of the soil,  $\varphi$  is the effective internal friction angle of the soil,  
 14 and  $r_s$  is the average unit weight of soil above the slip surface.  $\varphi^b$  is related to the matric suction;  
 15 when the matric suction is low, it is close to the internal friction angle(Zhang et al., 2018).  $D_s$  is the  
 16 thickness of the soil layer above the slip surface.  $u_s$  represent the matric suction, which can be  
 17 described by the Van Genuchten model(Van Genuchten, 1980):

$$18 \quad S_e = \frac{\theta - \theta_r}{\theta_s - \theta_r} = \left[ \frac{1}{1 + (\alpha_w \times u_s)^n} \right]^m \quad (8)$$

19 Where  $S_e$  represents the saturation degree,  $\theta$  denotes the soil water content of the HSU,  $\theta_s$  and  $\theta_r$  are  
 20 the saturated and residual water content, respectively. The parameters  $\alpha_w$ ,  $n$  and  $m$  characterize the  
 21 shape of the soil–water characteristic curve, with the relationship  $n=1-1/m$  .



1  
 2 Figure 3 HSU instability probability calculation diagram a. Extraction of HSU boundary points; b. Profile line  
 3 extraction of HSU polygon; c. Random search for critical slip surface; d. Enlarged view of the sliding mass for  
 4 detailed visualization.

5 (3)  $HSU_{prob}$  calculation

6 According to the saturated-unsaturated rainfall infiltration theory, the mechanical parameters  
 7 of the soil (such as cohesion force  $c(kPa)$  and internal friction angle  $\varphi(^{\circ})$ ) are significantly affected  
 8 by soil moisture content fluctuations. The variation in soil mechanical parameters during the  
 9 process of rainfall infiltration is very complex, and it is generally acknowledged that dry soil prior  
 10 to rainfall infiltration exhibits higher mechanical strength (characterized by elevated parameter  
 11 values). As rainwater continues to infiltrate, the soil water content gradually increases, leading to a  
 12 decreasing trend in mechanical parameters, such as cohesion and internal friction angle.  
 13 Consequently, the mechanical parameters of the soil within each HSU are not fixed, but spatial  
 14 uncertainty exists to some extent. In this context, employing probabilistic analysis methods to  
 15 calculate the instability probability of an HSU is a more reasonable choice. Probability density  
 16 functions (such as normal or uniform distributions) are commonly used to describe the uncertainty  
 17 of the geotechnical parameters. The normal distribution is considered suitable for small areas or  
 18 watersheds where hydrogeological parameters can be collected in detail, whereas a uniform  
 19 distribution is more applicable for larger areas, where it is difficult to acquire detailed  
 20 hydromechanical parameters(Wang et al., 2021; Wang et al., 2023).

1 In this study, we utilized a uniform distribution to simulate the uncertainty of the mechanical  
 2 parameters within the HSUs. The soil mechanical parameters in the unsaturated state before rainfall  
 3 were taken as the upper bound, while those in the fully saturated state were considered the lower  
 4 bound, thereby establishing the upper and lower value boundaries for the mechanical parameters  
 5 within the HSU, as indicated in Equations (9) and (10):

$$6 \quad c \in [c_{lower}, c_{upper}] \quad (9)$$

$$7 \quad \varphi \in [\varphi_{lower}, \varphi_{upper}] \quad (10)$$

8 where  $c_{upper}$  and  $c_{lower}$  represent the upper and lower bounds of  $c$ (kPa), respectively,  $\varphi_{upper}$  and  
 9  $\varphi_{lower}$  represent the upper and lower bounds of  $\varphi$ (°), respectively. The Monte Carlo method was  
 10 employed to randomly select the values within these bounds. The instability probability of the HSU  
 11 was calculated using Equation (11).

$$12 \quad HSU_{prob} = \frac{Sum_{F_s < 1}}{m} \quad (11)$$

13 where  $m$  represents the number of random selections for the mechanical parameters and  $m$   
 14 is set to 500.

#### 15 **2.4 The obtainment of key fitting parameters $\alpha$ and $\beta$ for I-D curves of HSUs**

16 In this study, an HSU is regarded as unstable when the value of  $HSU_{prob}$  exceeds 50%. Then,  
 17 the rainfall intensity and duration data with HSU instability under different rainfall scenarios were  
 18 recorded to obtain the key fitting parameters  $\alpha$  and  $\beta$  for the I-D curves of each HSU, thereby  
 19 establishing a database of parameters  $\alpha$  and  $\beta$ . The detailed steps are as follows.

##### 20 (1) Setting the antecedent effective rainfall levels $AER\_i(i=1,2,3\dots n)$

21 The antecedent effective rainfall(AER) has a significant impact on landslide occurrence.  
 22 Previous research indicates that in the Three Gorges Reservoir area, the minimum value of AER  
 23 before landslide occurrence is 0 mm, whereas the maximum value of AER can exceed 170  
 24 mm(Wang et al., 2021). Therefore, 20 different levels of AER ranging from 0 to 200 mm were  
 25 established with intervals of 10 mm.

##### 26 (2) Design of the combination of rainfall intensity (I) and duration(D)

27 For each antecedent rainfall level, we categorized rainfall intensity (I) into eight levels to  
 28 represent the variation from light to heavy rainstorms: 2, 5, 10, 20, 30, 40, 50, and 60 mm/h. The  
 29 rainfall duration (D) ranged from 1 to 24 h, with intervals of one hour. Consequently, 192

1 combinations of I and D were generated for each AER level.

2 (3) Generation of fitting parameters  $\alpha$ ,  $\beta$  of the I-D curves

3 For each combination of rainfall intensity and duration data, the method outlined in Section  
4 2.2 is used to determine the soil water distribution within each HSU, and the corresponding value  
5 of  $HSU_{prob}$  was computed using the method described in Section 2.3. If the HSU is unstable, the  
6 corresponding intensity and duration data can serve as data points for fitting the I-D curves.  
7 Subsequently, a power function was utilized to fit these data points to obtain the key fitting  
8 parameters  $\alpha$  and  $\beta$  of the I-D curve. As presented above, the fitting parameters  $\alpha$  and  $\beta$  for the I-D  
9 curve of each HSU can be generated, thereby establishing a database for  $\alpha$  and  $\beta$  at different AER  
10 levels.

### 11 **2.5 Warning Mode**

12 In practical applications, the antecedent effective rainfall(AER), rainfall intensity (I), and  
13 duration (D) for each HSU can be computed using Quantitative Precipitation Estimation (QPE) and  
14 Quantitative Precipitation Forecasting (QPF) products provided by the meteorological department  
15 (Wang et al., 2021). Next, we analyzed the relationship between the actual value of AER and the 20  
16 levels of AER documented in the database, thereby determining the level that is closest to the  
17 antecedent effective rainfall data of the HSU. The  $\alpha$  and  $\beta$  values corresponding to this level were  
18 retrieved from the database for the following assessments.

19 (1) If  $I \geq \alpha D^\beta$ , the data point (I, D) is above the warning curve; thus, the warning should be  
20 released.

21 (2) Conversely, if  $I < \alpha D^\beta$ , it signifies that the data point (I, D) is below the warning curve;  
22 therefore, no warning should be issued.

23 The programming languages Fortran 95 and Python 3.1 were employed to compile the  
24 algorithms outlined in Sections 2.1-2.5, and the overall flowchart of the warning mode is depicted  
25 in Figure 4.

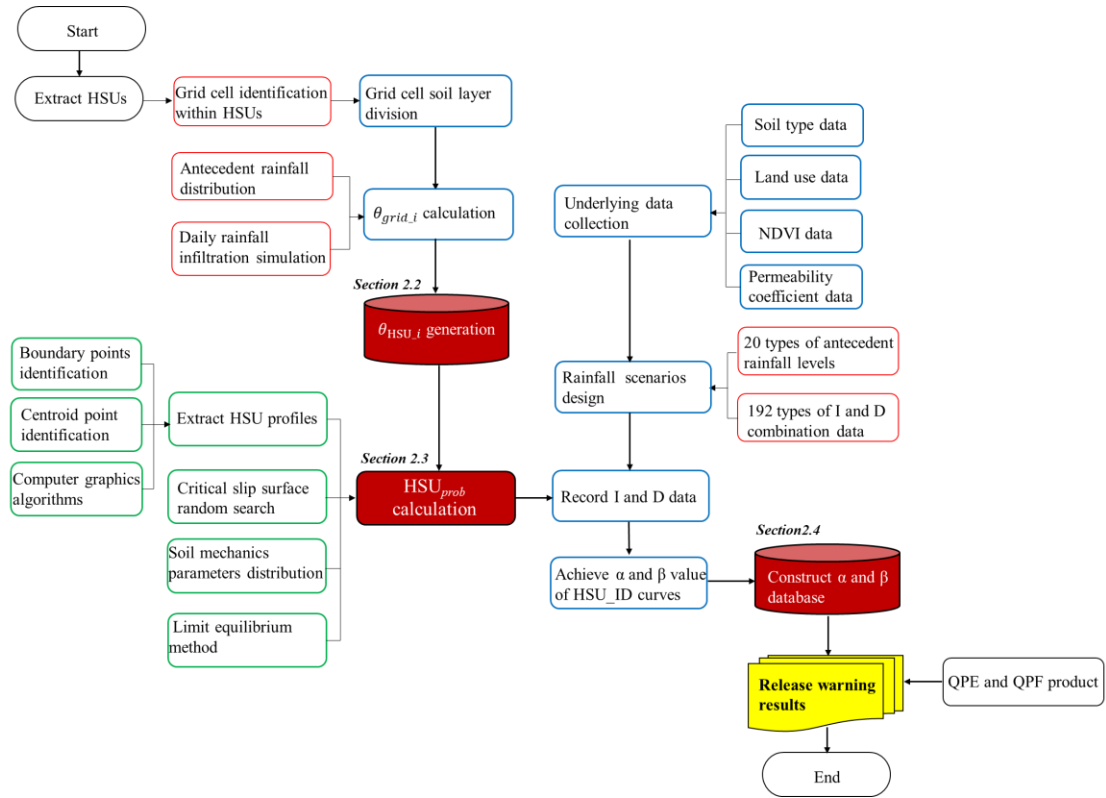


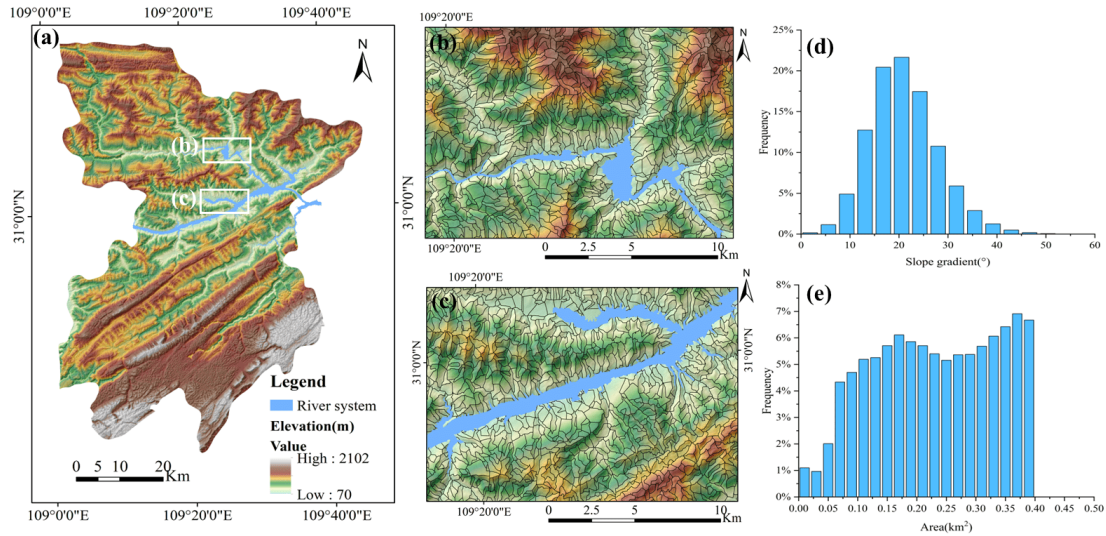
Figure 4 The flow chart of the fast warning mode based on parameter  $\alpha$  and  $\beta$  database

### 3 Study area and data

#### 3.1 Study area and slope unit data

Fengjie County is situated in the eastern region of the Three Gorges Reservoir area, with geographical coordinates ranging from  $109^{\circ}1'17''$  " to  $109^{\circ}45'58''$  East and  $30^{\circ}29'19''$  to  $31^{\circ}22'33''$  North, covering a total area of 4087 km<sup>2</sup>. The region has a subtropical humid monsoon climate with an annual average rainfall of 1,500–2,000 mm. The rainy season occurs from May to September, accounting for 70% of the annual precipitation. The terrain is primarily mountainous and the Yangtze River flows across the region from west to east. Geological hazards, such as landslides, debris flows, and collapses, are widely distributed in Fengjie County, with rainfall landslides posing the most significant threat. Based on the 7m DEM of Fengjie (Figure 5a), the MIA-HSU method was employed to extract the slope units, resulting in the identification of 17,547 HSUs (Figures 5 b and c). Histograms of the slope gradient and area distribution of the HSUs are presented in Figure 5d-e. As shown in Figure 5d, the slope gradients of the HSUs follow a normal distribution, with 85.4% of the slopes falling within the range of  $10^{\circ}$  to  $30^{\circ}$ . Figure 5e illustrates that the average area of the HSUs is 0.23 km<sup>2</sup>, with 53.9% of the slope units having an area less than 0.25 km<sup>2</sup>. Because the sliding depth of shallow landslides typically ranges from 2 m to 3 m, the majority of

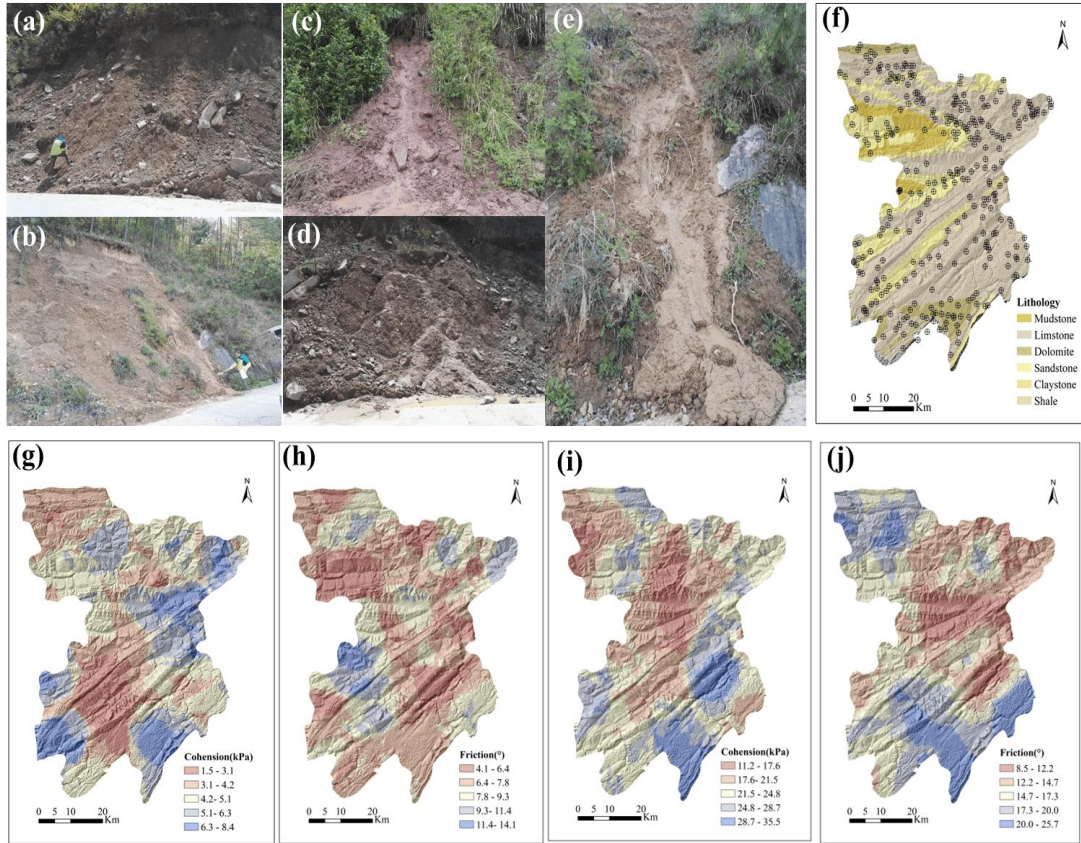
1 HSUs can be classified as small-to medium-scale landslides (with volumes under 500,000 m<sup>3</sup>).



2  
3 Figure 5 Division of HSUs in Fengjie County a. Fengjie DEM; b and c. Extraction results for selected regions:  
4 Enlarged View; d. Histogram of slope distribution of HSUs; e. Histogram of area distribution of HSUs.

### 5 3.2 Soil mechanical parameter $c$ (kPa) and $\phi$ ( $^{\circ}$ ) data of HSUs

6 The rainfall-triggered shallow landslides within the study area are mainly composed of  
7 quaternary clay and silt, which are classified as fine-grained soils(Wang et al., 2021; Wang et al.,  
8 2023). Field investigations indicate that the sliding soil is fully or even oversaturated, with some  
9 soil mass transitioning into mudflow during the sliding process. The laboratory moisture content  
10 tests revealed that the soil water content under these conditions approached or exceeded the liquid  
11 limit. To obtain detailed soil mechanical parameters under different moisture states, we conducted  
12 extensive field sampling across Fengjie County, resulting in 312 sampling points, as depicted in  
13 Figure 6f. For each sampling point, direct laboratory shear tests were performed to derive the soil  
14 mechanical parameters  $c$  (kPa) and  $\phi$  ( $^{\circ}$ ) at the liquid and plastic limits, respectively. Based on  
15 geological survey data provided by the Fengjie County Land Bureau, the dry density of soil within  
16 a 10-meter thickness ranges from 1.7 to 1.8 g/cm<sup>3</sup>(Wang et al.,2021). Therefore, the dry density of  
17 each soil samples is randomly selected within this range. In accordance with the ASTM-d6528  
18 (ASTM, 2017) standard, 312 groups of liquid-plastic limit tests and 624 groups of undrained direct  
19 shear tests were performed to obtain the mechanical parameters of each sample at both the liquid  
20 and plastic limit water contents. Subsequently, ArcGIS spatial analysis tools were utilized to  
21 generate distribution maps of  $c$  (kPa) and  $\phi$  ( $^{\circ}$ ) under plastic and liquid limit moisture conditions,  
22 as shown in Figures 6g-j.



1  
2 Figure 6 State of Landslide Soil Before and After Rainfall (a. Soil approaching plastic limit moisture content before  
3 rainfall; b. Soil approaching plastic limit moisture content before rainfall; c. Soil in a fluid state after rainfall; d. Soil  
4 in a fluid state after rainfall; e. Fully saturated and liquefied soil after rainfall; f. Soil sampling locations; g.  $c$  (kPa)  
5 at plastic limit moisture content; h.  $\phi$  (°) at plastic limit moisture content; i.  $c$  (kPa) at liquid limit moisture content;  
6 j.  $\phi$  (°) at liquid limit moisture content.)

### 7 3.3 Rainfall data

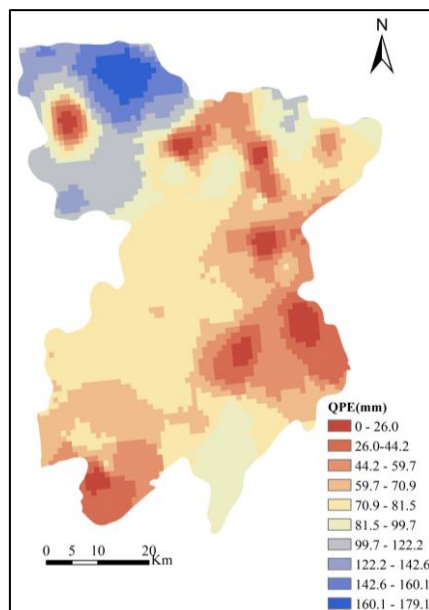
8 Rainfall data sources include Quantitative Precipitation Forecasting (QPF) products and  
9 Quantitative Precipitation Estimation (QPE) products. The QPF product obtained from the local  
10 government of Fengjie County is typically utilized to forecast future rainfall at a regional scale,  
11 which can provide rainfall forecast products for the next hour. QPE data are applied to estimate  
12 historical regional rainfall at a regional scale and are essential for determining the antecedent  
13 effective rainfall (AER), which can be computed as follows:

$$14 \quad AER = \sum_{i=1}^n a^n R_i \quad (12)$$

15 Where AER is the antecedent effective rainfall,  $a$  is the attenuation coefficient, which is equal  
16 to 0.84, based on the research of the Fengjie count (Wang et al., 2021),  $n$  is the number of days  
17 before the landslide occurs.

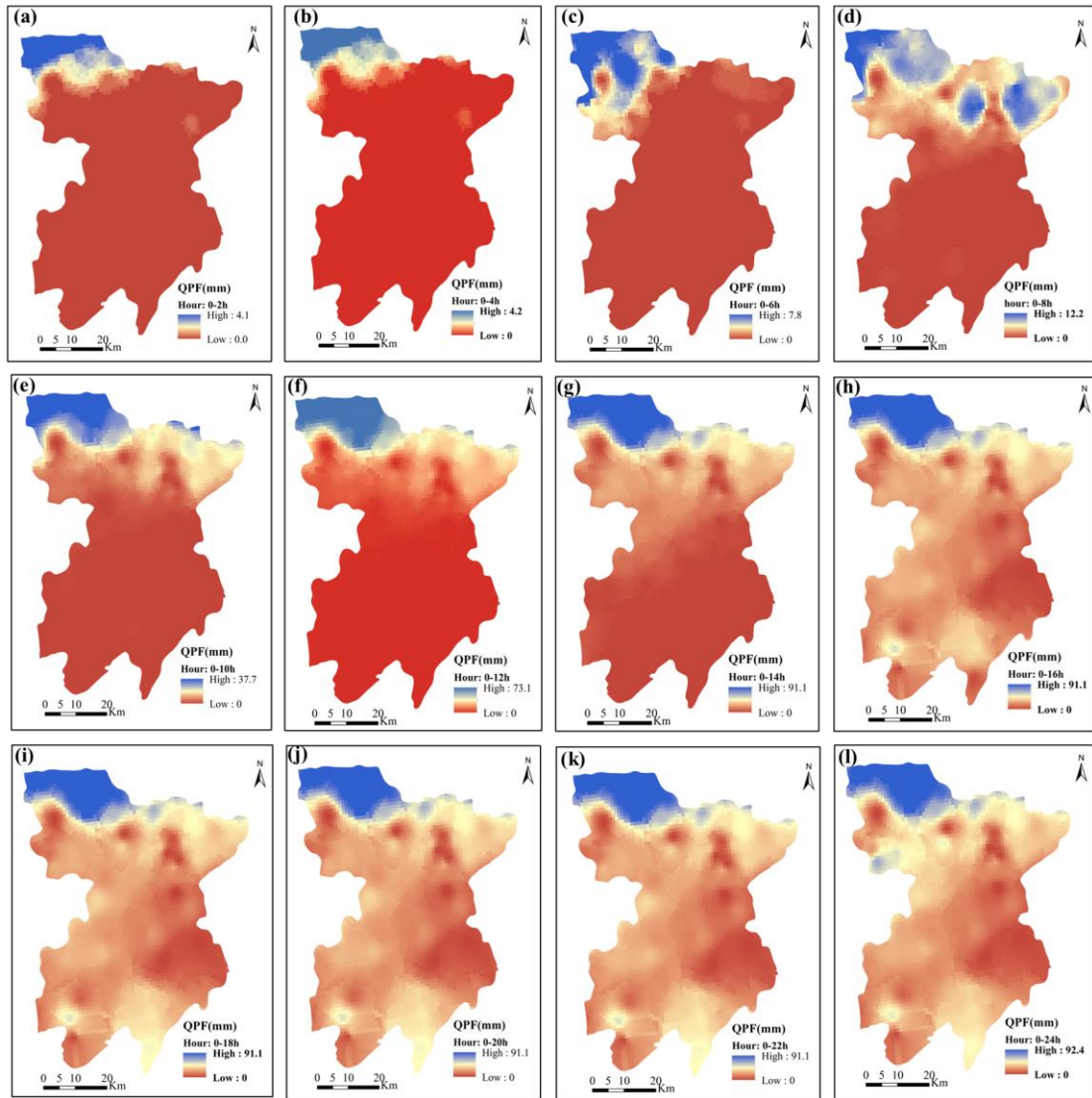
1 **4 Case study: Rainfall-induced landslides of 31 August, 2014**

2 From August 30–31, 2014, Fengjie experienced continuous heavy rainfall, triggering a series  
3 of landslide hazards that resulted in over 30 fatalities and an economic loss of 580 million yuan.  
4 Based on the daily QPE data for August 15-31, the effective precipitation for the 15 days prior to  
5 the landslide hazards is shown in Figure 7. As illustrated in Figure 7, the maximum precipitation  
6 during this period was 179.10 mm, which occurred in the northwestern region of the area. The  
7 hourly QPF data for August 31 are presented in Figure 8 *a-l*. As illustrated in Figure 8 *a-d*, the  
8 rainfall was minimal from 00:00 to 08:00, with a maximum cumulative rainfall of 12.2 mm 08:00.  
9 As shown in Figures 8e-g, rainfall began to increase rapidly at 10:00, reaching a maximum  
10 cumulative precipitation of 92.40 mm by 14:00 in the northwestern region of Fengjie County.  
11 Figures 8 h-l indicate that from 16:00 to 24:00, the cumulative rainfall remained constant,  
12 suggesting that the rainfall process had ceased.



13

14 Figure 7 Precipitation Data Processing (Effective Precipitation from August 15 to August 30, 2014)

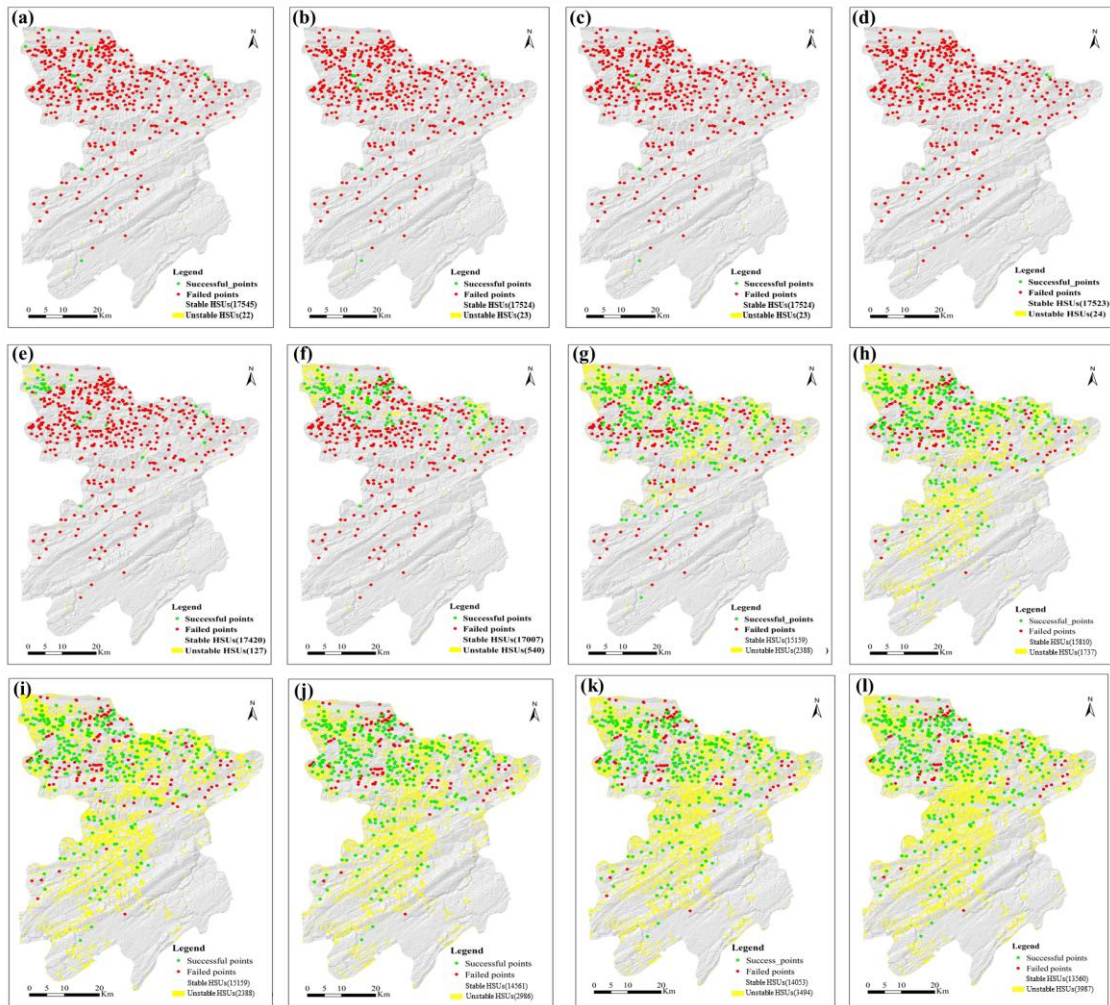


1  
 2 Figure 8 Radar forecast precipitation data for 2014/08/31 (a. 2:00; b. 4:00; c. 6:00; d. 8:00; e. 10:00; f. 12:00; g.  
 3 14:00; h. 16:00; i. 18:00; j. 20:00; k. 22:00; l. 24:00)

4 The Land and Resources Bureau of Fengjie County provided data on landslide points  
 5 triggered by rainfall on August 31. This heavy precipitation triggered 583 landslides, which were  
 6 mainly distributed in the northwestern region (as indicated by the red and green solid points in  
 7 Figure 9). This study utilized the QPE (Figure 7) and QPF data (Figures 8 a-l) as inputs to forecast  
 8 landslide hazards for August 31.

9 The landslide forecast results from 02:00 to 24:00 are shown in Figures 9(a-l). It can be seen  
 10 from Figures 8 and 9 that there is a good correlation between the spatial distribution of unstable  
 11 HSUs and rainfall characteristics. As presented in Figures 9a-d, at the beginning of the rainfall  
 12 process (before 8:00), the majority of the HSUs remained stable owing to the minimal rainfall.  
 13 Unstable HSUs began to emerge in the northwestern region starting at 10:00, coinciding with the

1 rapid increase in rainfall. Additionally, as the rainfall progressed, the number of unstable HSUs  
 2 increased swiftly and spread towards the central and southern regions (Figures 9f-g). Notably, many  
 3 unstable slope units appeared within several hours after heavy rainfall ceased. Figures 9h-l reveal  
 4 that from 16:00 to 24:00, although the heavy rainfall essentially ended, the number of unstable HSUs  
 5 continued to rise because of the moisture infiltration of the saturated top soil, reaching a total of  
 6 3,987 at 24:00.



7  
 8 Figure 9 Prediction results at 02:00 to 24:00 (a. 2:00; b. 4:00; c. 6:00; d. 8:00; e. 10:00; f. 12:00; g. 14:00; h. 16:00;  
 9 i. 18:00; j. 20:00; k. 22:00; l. 24:00)

10 This study employs the Receiver Operating Characteristic (ROC) method to analyze the  
 11 predictive performance of the HSU(Fawcett, 2006). For physically model-based slope units, the  
 12 ROC method describes the following four possible states using a contingency table:

- 13 ① True Positive (TP): HSU contain landslide points and exhibit instability;  
 14 ② True Negative (TN): HSU does not contain landslide points and does not exhibit instability;

1 ③ False Positive (FP): HSU does not contain landslide points but exhibits instability;

2 ④ False Negative (FN): HSU contains landslide points but does not exhibit instability.

3 According to GIS spatial statistics, 583 landslides triggered by rainfall on August 31 were  
4 contained within 425 HSUs. In this study, these HSUs are taken as benchmark values for the  
5 calculation of TP, TN, FP, and FN, and the missing alarm rate (MAR) and false alarm rate (FPR)  
6 can be calculated as follows:

$$7 \qquad \text{MAR} = 100\% \times \text{FN} / 425 \qquad (13)$$

$$8 \qquad \text{FPR} = 100\% \times \text{FP} / (\text{FP} + \text{TN}) \qquad (14)$$

9 The detailed forecast results for–02–24h are shown in Table 1. As shown in columns 7–8 of  
10 Table 1, with increasing rainfall duration, the Missing Alarm Rate (MAR) gradually decreases,  
11 while the False Positive Rate (FPR) gradually increases. Taking the result of 24h as an example, the  
12 MAR of 24h is 11.8% and the FPR is 21.1%, indicating that the prediction result can satisfy the  
13 requirement of early warning practice.

14 Table 1 Analysis of Forecast Results for the 831 Case Study

Forecasting hour(h)	Unstable HSUs	TP	TN	FP	FN	MAR (%)	FPR (%)
02	22	7	17097	25	418	98.4	0.1
04	23	3	17102	20	422	99.3	0.1
06	23	3	17102	20	422	99.3	0.1
08	24	2	17100	22	423	99.5	0.1
10	127	27	17022	100	398	93.6	0.6
12	540	116	16698	424	309	72.7	2.5
14	1370	231	15983	1139	194	45.6	6.7
16	1737	289	15674	1448	136	32.0	8.5
18	2388	327	15061	2061	98	23.1	12.0
20	2986	354	14490	2632	71	16.7	15.4
22	3494	364	13992	3130	61	14.4	18.3
24	3987	375	13510	3612	50	11.8	21.1

15 According to the ROC method, the precision and accuracy of the prediction results were  
16 calculated as follows:

$$17 \qquad \text{Precision} = \text{TPR} / (\text{TPR} + \text{FPR}) \qquad (15)$$

$$18 \qquad \text{Accuracy} = (\text{TP} + \text{TN}) / (\text{TP} + \text{FN} + \text{TN} + \text{FP}) \qquad (16)$$

19 Table 2 provide the calculation results of precision and accuracy at 24h. As shown, the  
20 precision of the forecasting results is 80.7%, with an accuracy value of 79.1%, indicating the  
21 proposed warning mode has satisfactory comprehensive forecasting performance.

1

Table 2 Calculation Results of Precision and Accuracy at the 24th Hour

Forecasting hour(h)	Unstable HSUs	TP	TN	FP	FN	Precision(%)	Accuracy(%)
24	3987	375	13510	3612	50	80.7	79.1

## 2 **5 Discussion**

### 3 **5.1 The discussion on the computational efficiency**

4 For emergency warnings during the rainy season, the swift release of warning information is  
 5 crucial for local authorities to develop emergency plans and to evacuate residents from landslide-  
 6 prone areas. Therefore, local governments not only seek satisfactory accuracy in the warning model  
 7 but also require minimal time. To evaluate the computational efficiency of the proposed model, a  
 8 standard laptop was utilized to execute the forecast for landslide hazards on August 31. The device  
 9 specifications and computation times are presented in Table 3. As shown in Table 3, for the regional  
 10 scale covering several thousand square kilometers, the prediction model can rapidly complete real-  
 11 time warnings for the next 24 h within 12 min, indicating that its computational efficiency can  
 12 satisfy the requirements of emergency warning.

13

Table 3 Analysis of computational efficiency of the prediction model

Area (m <sup>2</sup> )	Number of HSU	CPU	System	Equipment name	Memory	Run time
4080	17547	Intel(R) Core i7	Windows 64-bit operating system	ThinkPad P15 Workstation	16G	<12min

### 14 **5.2 Further analysis of prediction performance**

15 Using the 24-hour prediction results as an example, we randomly selected seven HSUs with  
 16 false alarms for further analysis(Table 4). Columns 3–5 of Table 4 present the effective antecedent  
 17 rainfall AER of these HSUs, the AER levels assigned by the database, and the relative errors,  
 18 respectively. As shown in Column 5, the relative error ranges from 0.7% to 6.3%, indicating that the  
 19 20 levels of the AER designed in the database can accurately reflect the effective antecedent rainfall  
 20 characteristics of the HSUs. The average rainfall intensity, duration, and cumulative rainfall data at  
 21 24:00 are shown in Columns 6–8. As seen in Column 6, the cumulative rainfall for the seven HSUs  
 22 ranges from 12 mm to 29.8 mm, with average rainfall intensities range from 0.5 mm/h to 1.25 mm/h,  
 23 which can be classified as light to moderate rain type. The instability probability ( $HSU_{prob}$ ) of these  
 24 HSUs was calculated to investigate the causes of false positives. As shown in Column 9, among the  
 25 seven HSUs with false alarms, five had an instability probability of less than 50%, indicating that

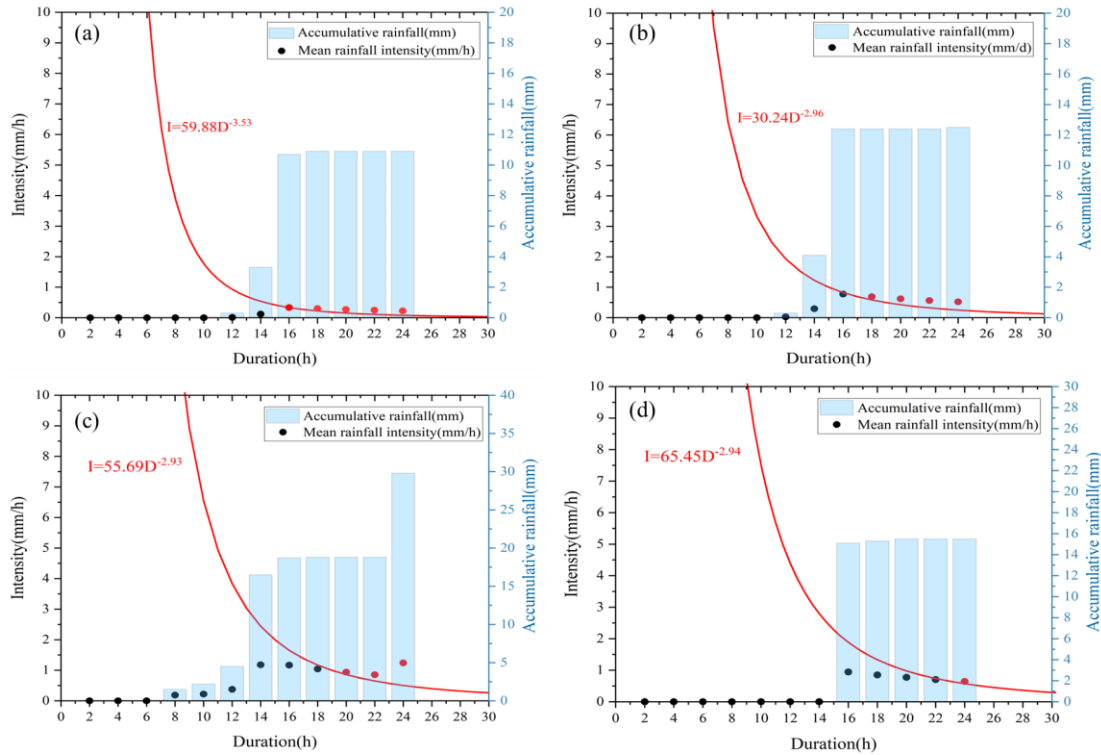
1 these HSUs did not experience instability during the rainfall process. Therefore, we cautiously  
 2 conclude that although the prediction model exhibits preferable operational efficiency, it may  
 3 increase the false-positive rate to some extent.

4 Table 4 The selected HSUs that report false alarms at 24:00

Number of HSUs	Slope gradient (°)	AER assignment			Daily accumulated rainfall (mm)	Duration (h)	Rainfall intensity $I$ (mm/h)	HSU <sub>prob</sub>
		Actual AER (mm)	AER levels assigned by the database (mm)	Relative error				
6172	19.4	74.6	70	6.2%	24.2	24	1.0	0.88
8561	26.5	70.9	70	1.3%	12.2	24	0.5	0.19
6066	26.7	83.1	80	3.7%	29.8	24	1.25	0.65
8535	25.9	68.6	70	2.0%	10.9	24	0.45	0.18
13108	40.3	74.1	70	5.5%	15.4	24	0.64	0.29
8297	23.4	70.5	70	0.7%	12.0	24	0.5	0.14
12966	38.3	74.7	70	6.3%	14.6	24	0.61	0.25

5 To investigate the potential for reducing the false-alarm rate, we selected four HSUs from Table  
 6 4 for further analysis. Figures 10 a-d presented the I-D curves and cumulative precipitation  
 7 distribution histograms for these HSUs.

8 For each HSU, the QPF data from 00:00 to 24:00 were discretized into 12 sets of rainfall  
 9 intensity and duration data points at 2-hour intervals (represented by black and red solid dots). The  
 10 black solid dots positioned below the I-D curve indicate that the HSU is stable at that moment,  
 11 whereas the red solid dots located above the curve signify false alarms at the current forecasting  
 12 hour. As shown in Figures 10a-d, the red false alarm points for the four HSUs are all situated very  
 13 close to the I-D curve, nearly tangent to it. This proximity suggests that slight spatial adjustments  
 14 to these points could alter the forecast results. Another important issue is that some of the black  
 15 solid dots correspond to a cumulative rainfall of 0 mm, indicating that the rainfall process had not  
 16 yet begun. Therefore, it is necessary to adjust the spatial positions of data points I and D based on  
 17 the actual initiation time of the rainfall process, thereby facilitating an in-depth investigation of the  
 18 causes of the false alarms.



1

2 Figure 10 The I-D Curves of HSUs before the adjustment of rainfall process (a. 8535; b. 8561; c. 6066; d. 13108)

3 In this study, an HSU with number 8535 is taken as an example to illustrate the process of  
 4 adjusting the spatial positions of data points I and D. As shown in Table 5, the rainfall process for  
 5 this HSU started at 12:00 and ended at 24:00 with a duration of 12 h. The start time of rainfall was  
 6 used as the starting point to recalculate the rainfall intensity during the rainfall process, as shown in  
 7 the bold text in Table 5. The adjusted average rainfall intensity was significantly higher than the  
 8 values prior to adjustment. This means that the adjustment of the rainfall process led to notable  
 9 changes in the spatial locations of the data points I and D. As shown in Figure 11a, after updating  
 10 the positions of data points I and D, the HSU does not exhibit any false alarms. Figures 11b-d present  
 11 the updated forecast results for the other three HSUs after the adjustment. As shown in Figure 11a-  
 12 d, following the adjustments, three out of these four HSUs were able to release accurate results.  
 13 Therefore, we advise that practical warning applications should consider the influence of the  
 14 difference in rainfall processes of HSUs on the prediction results.

15

16

17

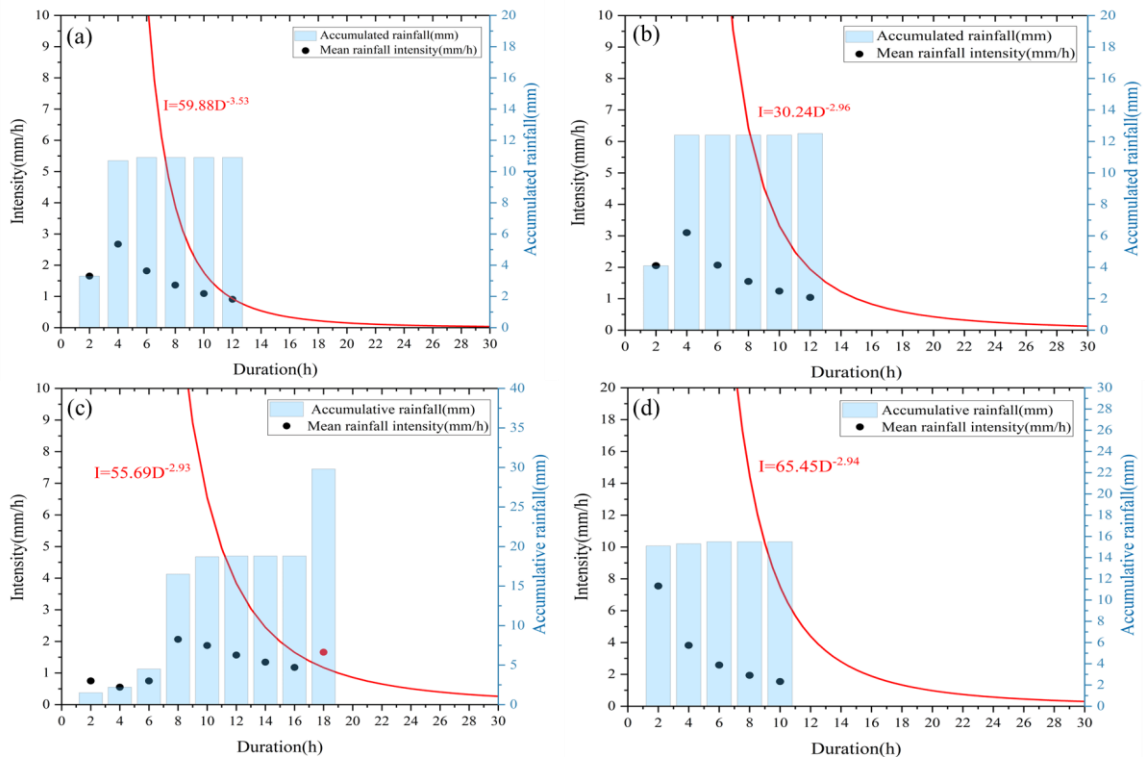
18

1

Table 5 Rainfall process adjustment for HSU with number of 8535

Time	2:0	4:0	6:0	8:0	10:0	12:0	14:0	16:0	18:0	20:0	22:0	24:0	
Accumulated rainfall(mm)	0	0	0	0	0	0.3	3.3	10.7	10.9	10.9	10.9	10.9	
Before adjustment	I(mm/h)	0	0	0	0	0	0.2	0.7	0.6	0.5	0.5	0.5	
	D (h)	2	4	6	8	10	12	14	16	18	20	22	24
After adjustment	I(mm/h)	/					<b>0</b>	<b>1.6</b>	<b>2.7</b>	<b>1.8</b>	<b>1.3</b>	<b>1.1</b>	<b>0.9</b>
	D (h)	/					<b>0</b>	<b>2</b>	<b>4</b>	<b>6</b>	<b>8</b>	<b>10</b>	<b>12</b>

2



3

4 Figure 11 The I-D Curves of HSUs after the adjustment of rainfall process (a. 8535; b. 8561; c. 6066; d. 13108)

5 **5.3 Comparison with existing approaches in the Fengjie county**

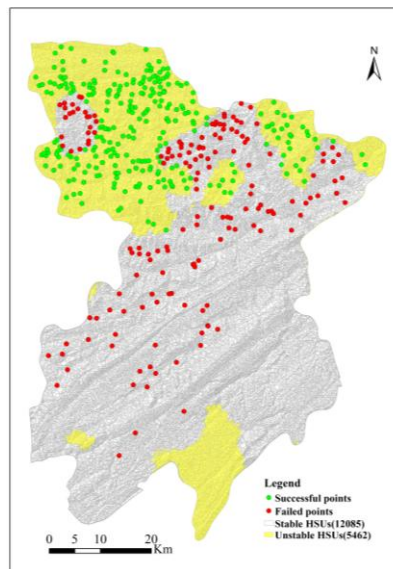
6 Statistical methods have been widely used to establish rainfall thresholds for landslides. Liu  
 7 (2024) categorized Chongqing into four distinct subregions based on topography, tectonic structures,  
 8 lithological stratigraphy, and the distribution and characteristics of landslides, and established the  
 9 rainfall thresholds for landslides in each subregion, as shown in Table 6. Fengjie county belongs to  
 10 Subregion II, with its rainfall threshold is listed in the second row of Table 6. In this table, R

1 represents the cumulative daily rainfall, while  $R_e$  signifies the antecedent effective rainfall.

2 Table 6 Equations of the thresholds defined for each subregion (Liu et al., 2024)

Threshold	5%	30%	50%	80%
Subregion I	$R = -1.13R_e + 43$	$R = -1.13R_e + 70$	$R = -1.13R_e + 85$	$R = -1.13R_e + 135$
Subregion II	$R = -0.93R_e + 38$	$R = -0.93R_e + 70$	$R = -0.93R_e + 100$	$R = -0.93R_e + 145$
Subregion III	$R = -0.96R_e + 40$	$R = -0.96R_e + 100$	$R = -0.96R_e + 135$	$R = -0.96R_e + 180$
Subregion IV	$R = -1.15R_e + 41$	$R = -1.15R_e + 76$	$R = -1.15R_e + 98$	$R = -1.15R_e + 140$

3 The prediction results derived from statistical methods are illustrated in Figure 12, with  
 4 detailed prediction performance parameters provided in Table 7. As depicted in Figure 12, there are  
 5 5,462 unstable HSUs, primarily located in the northwest and southern mountainous regions.  
 6 According to Table 7, 256 landslide events are successfully predicted by Liu’s model. However, the  
 7 statistical method exhibits a missing alarm rate of 40% and a false alarm rate of 30.4%, resulting in  
 8 low overall precision and accuracy. In contrast, the missing and false alarm rate of the HSU\_ID  
 9 model are 11.8% and 21.1% at the 24<sup>th</sup> hour (Table 1), thus demonstrating superior forecasting  
 10 performance.



11 Figure 12 Prediction outcomes generated by Liu’s model

12 Table 7 Prediction performance parameters of Liu’s model

Unstable HSUs	TP	TN	FP	FN	MAR (%)	FPR (%)	Precision(%)	Accuracy(%)
5462	256	11915	5206	170	40.0	30.4	66.4	69.4

#### 1 **5.4 Limitations and future work**

2 The method proposed in this paper reduces dependence on landslide inventory data and avoids  
3 the issue of excessive computation time associated with physical models. This offers promising  
4 application prospects for emergency early warning in regions of third-world countries where  
5 landslide inventory data are scarce. However, it should be noted that the calculation of  $HSU_{prob}$  relies  
6 on regional-scale mechanical parameters. Therefore, establishing the distribution of mechanical  
7 parameters in Southwest China through field sampling, experiments, and spatial analysis is an  
8 important task for the future. Another important task lies in optimizing the model algorithm, because  
9 the physical mechanisms of rainfall landslides are extremely complex, and the soil-water coupling  
10 process under rainfall involves significant nonlinearity (Apir et al., 2010). Some machine learning  
11 methods that incorporate physical frameworks are expected to accurately describe this issue (for  
12 example the PINN) . .Therefore, improving the model algorithm by combining machine learning  
13 with physical approaches is another important task for the future.

#### 14 **6 Conclusion**

15 Currently, the operational forecasting of rainfall-induced landslides over regional scales of  
16 thousands of square kilometers faces significant challenges. Conventional physical and statistical  
17 approaches have shown limitations in terms of achieving satisfactory results. This study utilized  
18 HSU as a basis to integrate physical models and rainfall threshold methods for a warning model  
19 applicable to large-scale regions. The warning model employs HSU as a prediction unit to improve  
20 the clarity of the warning results, physical methods are utilized to develop the warning criteria,  
21 thereby reducing the overreliance on historical observational data, and a database of rainfall  
22 parameters across different rainfall scenarios is constructed, which enhances the efficiency and  
23 applicability of the warning model. The prediction performance was validated through a case study  
24 of “8.31” rainfall landslides in Fengjie County. The conclusions are as follows.

25 (1) A rainfall-triggered landslide warning model was established by integrating HSUs, physical  
26 approaches, and rainfall parameters. Initially, a grid-based HSU hydrological analysis technique  
27 was established to determine the soil moisture content distribution within the HSUs during different  
28 rainfall hours. Subsequently, computer graphics algorithms, random search techniques, and  
29 infinite slope models were used to develop a regional-scale HSU stability analysis method. Soil  
30 mechanics parameters at the limit of water content and probability density functions were used to

1 describe the spatial uncertainty of the soil mechanical parameters within the HSU during rainfall  
2 infiltration, allowing for the calculation of the instability probability of the HSU. Different rainfall  
3 scenarios were simulated to derive rainfall intensity  $I$  and duration  $D$  data that can trigger HSU  
4 instability, thereby constructing early warning curves for the rainfall thresholds of the HSU.

5 (2) A database for the I-D curve fitting parameters  $\alpha$  and  $\beta$  across various AER levels was  
6 established. This database includes  $\alpha$  and  $\beta$  data for 17,547 HSUs across 20 AER levels, amounting  
7 to a total of 350,940 records, thus offering substantial data support for rainfall-induced landslide  
8 predictions in Fengjie County. In practical applications, it is sufficient to quickly issue warning  
9 information by assessing the relationship between the values of  $I$  and  $\alpha D^\beta$ , thereby reducing the time  
10 required to calculate the safety factors using conventional physical models. The calculation  
11 efficiency test indicates that the warning mode can perform forecasts for thousands of kilometers  
12 within a runtime of less than 12 min, thereby meeting the operational needs for real-time warnings  
13 over large regional scales.

14 (3) The case study indicates that the distribution trends of unstable HSUs align well with  
15 rainfall characteristics. As the rainfall duration increased, the missing alarm rate (MAR) gradually  
16 decreased, while the false alarm rate (FAR) continued to increase. Taking the 24-hour forecast  
17 results as an example, the missing alarm rate was 11.8%, while the false alarm rate was 21.1%. ROC  
18 analysis revealed that the accuracy of the forecast result at this moment was 80.7%, with a precision  
19 of 79.1%, reflecting satisfactory overall forecasting performance. Further discussion of the false  
20 alarm rate suggests that adjusting the spatial locations of rainfall intensity and duration data points  
21 based on the rainfall characteristics of each HSU may be conducive to reducing false alarm rates.

## 22 23 24 25 26 27 **Acknowledgements**

28 The authors would like to acknowledge the Chongqing Meteorological Bureau, China for providing  
29 the QPE and QPF data free of charge. We are also thankful to the Land and Resources Bureau of  
30 Fengjie county for their support with the field investigation.

## 31 32 **Conflict of Interest Statement**

1 All authors declare that they have no conflicts of interest. We declare that we do not have any  
2 commercial or associative interests that represent a conflict of interest in connection with the  
3 submitted work.

#### 4 **Author contributions**

6 **KW:** Conceptualization, Writing – original draft, Supervision, Data curation Funding acquisition;  
7 **LX:** Supervision, Visualization, Writing – original draft; **SX:** Investigation, Data curation,  
8 Validation; **SZ:** Methodology, Resources, Validation; **YJ:** Supervision, Validation, Software; **JZ:**  
9 Investigation, Software; **HG:** Investigation, Visualization; **LZ:** Project administration, Visualization;  
10 **ZW:** Project administration, Writing – review & editing; **FQ:** Writing – review & editing.

#### 11 **Disclosure statement**

12 No potential conflict of interest was reported by the author(s).

#### 13 **Funding**

14 This work was supported by the [National Natural Science Foundation of China] under Grant  
15 [42301083]; and the Training Program for Young Backbone Teachers in Higher Education  
16 Institutions of Henan Province[2025GGJS094]; and [General Project of Henan Province Education  
17 Science Planning, China] under Grant [2025YB0116].

#### 18 **Data availability statement**

19 The datasets supporting this study are available from the corresponding author upon reasonable  
20 request.

#### 21 **Reference**

- 22 Alvioli, M., Guzzetti, F., & Marchesini, I. 2020. Parameter-free delineation of slope units and t  
23 errain subdivision of Italy. *Geomorphology*, 358, 107124. <https://doi.org/10.1016/j.geomorph.2020.107124>.
- 24 Aristizábal, E., Vélez, J. I., Martínez, H. E., & Jaboyedoff, M. 2016. SHIA\_Landslide: a distri  
25 buted conceptual and physically based model to forecast the temporal and spatial occur  
26 rence of shallow landslides triggered by rainfall in tropical and mountainous basins. *La  
27 ndslides*, 13(3), 497-517. <https://doi.org/10.1007/s10346-015-0580-7>.
- 28 ASTM D6528-17. (2017). Standard test method for consolidated undrained direct simple shear t  
29 esting of fine grain soils. ASTM International: West Conshohocken, PA, USA
- 30 Apip, Takara K, Yamashiki Y, Sassa K, Bagiawan Ibrahim A, and Fukuoka H, 2010. A distributed  
31 hydrological-geotechnical model using satellite-derived rainfall estimates for shallow landslide  
32 prediction system at a catchment scale, *Landslides*, 7: 237–258.
- 33 Baum, R. L., Savage, W. Z., & Godt, J. 2008. TRIGRS—a Fortran program for transient rainf  
34 all infiltration and grid-based regional slope-stability analysis. US Geological Survey O  
35 pen File Report 2008-1159, 2.
- 36 Bezak, N., Šraj, M., & Matjaž, M. 2016. Copula-based IDF curves and empirical rainfall thres  
37 holds for flash floods and rainfall-induced landslides. *Journal of Hydrology*, 541, 272-2  
38 84. <https://doi.org/10.1016/j.jhydrol.2016.02.058>.

- 1 Bogaard, T., & Greco, R. 2018. Invited perspectives: Hydrological perspectives on precipitation  
2 intensity-duration thresholds for landslide initiation: proposing hydro-meteorological thre  
3 sholds. *Natural Hazards and Earth System Sciences*, 18, 31-39. [https://doi.org/10.5194/n](https://doi.org/10.5194/nhess-18-31-2018)  
4 [hess-18-31-2018](https://doi.org/10.5194/nhess-18-31-2018).
- 5 Brunetti, M., Peruccacci, S., Rossi, M., S, L., Valigi, D., & Guzzetti, F. 2010. Rainfall threshol  
6 ds for the possible occurrence of landslides in Italy. *Natural Hazards and Earth System*  
7 *Sciences*, 10. <https://doi.org/10.5194/nhess-10-447-2010>.
- 8 Cuomo, S., Di Perna, A., & Martinelli, M. 2021. Modelling the spatio-temporal evolution of a  
9 rainfall-induced retrogressive landslide in an unsaturated slope. *Engineering Geology*, 29  
10 4, 106371. <https://doi.org/10.1016/j.enggeo.2021.106371>.
- 11 Domènech, G., Alvioli, M., & Corominas, J. 2019. Preparing first-time slope failures hazard m  
12 aps: from pixel-based to slope unit-based. *Landslides*, 17, 249-265. [https://doi.org/10.10](https://doi.org/10.1007/s10346-019-01279-4)  
13 [07/s10346-019-01279-4](https://doi.org/10.1007/s10346-019-01279-4).
- 14 Fawcett, T. 2006. Introduction to ROC analysis. *Pattern Recognition Letters*, 27, 861-874. [https:](https://doi.org/10.1016/j.patrec.2005.10.010)  
15 [//doi.org/10.1016/j.patrec.2005.10.010](https://doi.org/10.1016/j.patrec.2005.10.010).
- 16 Greco, V. 1996. Efficient Monte Carlo Technique for Locating Critical Slip Surface. *Journal of*  
17 *Geotechnical Engineering*, 122, 517-525. [https://doi.org/10.1061/\(ASCE\)0733-9410\(1996\)1](https://doi.org/10.1061/(ASCE)0733-9410(1996)122:7(517))  
18 [22:7\(517\)](https://doi.org/10.1061/(ASCE)0733-9410(1996)122:7(517)).
- 19 Gu, T., Wang, J., Fu, X., & Liu, Y. 2014. GIS and limit equilibrium in the assessment of regi  
20 onal slope stability and mapping of landslide susceptibility. *Bulletin of Engineering Ge*  
21 *ology and the Environment*, 74, 1-11. <https://doi.org/10.1007/s10064-014-0689-2>.
- 22 Guo, Z., Torra, O., Hürlimann, M., Abancó, C., & Medina, V. 2022. FSLAM: A QGIS plugin  
23 for fast regional susceptibility assessment of rainfall-induced landslides. *Environmental*  
24 *Modelling & Software*, 150, 105354. <https://doi.org/10.1016/j.envsoft.2022.105354>.
- 25 He, X., Hong, Y., Vergara, H., Kirstetter, P.-E., Gourley, J., Zhang, Y., Qiao, G., & Liu, C. 20  
26 16. Development of a Coupled Hydrological-geotechnical Framework for Rainfall-induc  
27 ed Landslides Prediction. *Journal of Hydrology*, 543. [https://doi.org/10.1016/j.jhydrol.201](https://doi.org/10.1016/j.jhydrol.2016.10.016)  
28 [6.10.016](https://doi.org/10.1016/j.jhydrol.2016.10.016).
- 29 Hong, M., Kim, J., & Jeong, S. 2017. Rainfall intensity-duration thresholds for landslide predic  
30 tion in South Korea by considering the effects of antecedent rainfall. *Landslides*, 15. [h](https://doi.org/10.1007/s10346-017-0892-x)  
31 [tps://doi.org/10.1007/s10346-017-0892-x](https://doi.org/10.1007/s10346-017-0892-x).
- 32 Hong, Y., Hiura, H., Shino, K., Sassa, K., Suemine, A., Fukuoka, H., & Wang, G. 2005. The  
33 influence of intense rainfall on the activity of large-scale crystalline schist landslides in  
34 Shikoku Island, Japan. *Landslides*, 2, 97-105. <https://doi.org/10.1007/s10346-004-0043-z>.
- 35 Huang, F., Tao, S., Chang, Z., Huang, J., Fan, X., Jiang, S.-H., & Li, W. 2021. Efficient and  
36 automatic extraction of slope units based on multi-scale segmentation method for lands  
37 lide assessments. *Landslides*, 18. <https://doi.org/10.1007/s10346-021-01756-9>.
- 38 Kanungo, D., & Sharma, S. 2014. Rainfall thresholds for prediction of shallow landslides arou  
39 nd Chamoli-Joshimath region, Garhwal Himalayas, India. *Landslides*, 11, 629-638. [https:](https://doi.org/10.1007/s10346-013-0438-9)  
40 [//doi.org/10.1007/s10346-013-0438-9](https://doi.org/10.1007/s10346-013-0438-9).
- 41 Kim, S., Chun, K., Kim, M., Catani, F., Choi, B., & Seo, J. I. 2020. Effect of antecedent rain  
42 fall conditions and their variations on shallow landslide-triggering rainfall thresholds in  
43 South Korea. *Landslides*, 18. <https://doi.org/10.1007/s10346-020-01505-4>.
- 44 Liang, W.-L., & Uchida, T. 2021. Performance and topographic preferences of dynamic and ste

- 1 ady models for shallow landslide prediction in a small catchment. *Landslides*, 19. <http://doi.org/10.1007/s10346-021-01771-w>.
- 2
- 3 Li, D., Wang, Z., Guo, H., Zhang, Y., Cheng, X., & Yu, Q. 2025. Deep Learning in Slope St  
4 ability Analysis: Evolution, Challenges, and Future Directions. *Geotechnical and Geolog  
5 ical Engineering*, 43(8), 1-48.
- 6 Liu SH, Du J, Yin KL, Zhou C, Huang CC, Jiang J, Yu J, 2024. Regional early warning mod  
7 el for rainfall induced landslide based on slope unit in Chongqing, China. *Engineering  
8 Geology*, 333: 107464.
- 9 Ma, T., Changjiang, L., Lu, Z., & Bao, Q. 2015. Rainfall intensity–duration thresholds for the  
10 initiation of landslides in Zhejiang Province, China. *Geomorphology*, 245. <https://doi.org/10.1016/j.geomorph.2015.05.016>.
- 11
- 12 Marra, F. 2018. Rainfall thresholds for landslide occurrence: systematic underestimation using c  
13 oarse temporal resolution data. *Natural Hazards*, 95. <https://doi.org/10.1007/s11069-018-3508-4>.
- 14
- 15 Medina, V., Hürlimann, M., Guo, Z., Lloret, A., & Vaunat, J. 2021. Fast physically-based mod  
16 el for rainfall-induced landslide susceptibility assessment at regional scale. *CATENA*, 2  
17 01, 105213. <https://doi.org/10.1016/j.catena.2021.105213>.
- 18 Montgomery, D., & Dietrich, W. 1994. A Physically Based Model for the Topographic Control  
19 on Shallow Landsliding. *Water Resources Research - WATER RESOUR RES*, 30, 1153  
20 -1172. <https://doi.org/10.1029/93WR02979>.
- 21 Montrasio, L., & Valentino, R. 2016. Modelling Rainfall-induced Shallow Landslides at Differe  
22 nt Scales Using SLIP - Part I. *Procedia Engineering*, 158, 476-481. <https://doi.org/10.1016/j.proeng.2016.08.475>.
- 23
- 24 Moeineddin, A., Seguí, C., Dueber, S., & Fuentes, R. 2023. Physics-informed neural networks a  
25 pplied to catastrophic creeping landslides. *Landslides*, 20(9), 1853-1863.
- 26 Pinho, T., & Augusto Filho, O. 2022. Landslide susceptibility mapping using the infinite slope,  
27 SHALSTAB, SINMAP, and TRIGRS models in Serra do Mar, Brazil. *Journal of Mou  
28 ntain Science*, 19, 1018-1036. <https://doi.org/10.1007/s11629-021-7057-z>.
- 29 Pradhan, A., Lee, S.-R., Kim, Y.-T. 2018. A shallow slide prediction model combining rainfall  
30 threshold warnings and shallow slide susceptibility in Busan, Korea. *Landslides*, 16: 6.  
31 47-659. doi: <https://doi.org/10.1007/s10346-018-1112-z>
- 32 Rigon, R., Bertoldi, G., & Over, T. 2006. GEOTop: A Distributed Hydrological Model with Co  
33 upled Water and Energy Budgets. *Journal of Hydrometeorology*, 7, 2006. <https://doi.org/10.1175/JHM497.1>.
- 34
- 35 Rosi, A., Segoni, S., Canavesi, V., Monni, A., Gallucci, A., & Casagli, N. 2020. Definition of  
36 3D rainfall thresholds to increase operative landslide early warning system performance  
37 s. *Landslides*, 18. <https://doi.org/10.1007/s10346-020-01523-2>.
- 38 Rossi, G., Catani, F., Leoni, L., Segoni, S., & Tofani, V. 2013. HIRESSES: a physically based s  
39 lope stability simulator for HPC applications. *Nat. Hazards Earth Syst. Sci.*, 13(1), 151  
40 -166. <https://doi.org/10.5194/nhess-13-151-2013>.
- 41 Tarboton, D., & Goodwin, C. 1970. The SINMAP approach to terrain stability mapping.
- 42 Tufano, R., Formetta, G., Calcaterra, D., & De Vita, P. 2021. Hydrological control of soil thic  
43 kness spatial variability on the initiation of rainfall-induced shallow landslides using a  
44 three-dimensional model. *Landslides*, 18. <https://doi.org/10.1007/s10346-021-01681-x>.

- 1 Turel, M., & Frost, J. (2011). *Delineation of Slope Profiles from Digital Elevation Models for*  
2 *Landslide Hazard Analysis*. [https://doi.org/10.1061/41183\(418\)87](https://doi.org/10.1061/41183(418)87)
- 3 Van Genuchten, M. 1980. A Closed-form Equation for Predicting the Hydraulic Conductivity of  
4 Unsaturated Soils. *Soil Science Society of America Journal*, 44. <https://doi.org/10.2136/sssaj1980.03615995004400050002x>.
- 5  
6 Wang, K., Xie, S., Zhang, S., Zhu, L., Ma, J., Liu, D., & Yang, H. 2024. Creating a big data  
7 source of landslide deformation stages: New thoughts on identifying displacement warn-  
8 ing thresholds. *Journal of Asian Earth Sciences*, 266, 106120. <https://doi.org/10.1016/j.jseaes.2024.106120>.
- 9  
10 Wang, K., & Zhang, S. 2021. Rainfall-induced landslides assessment in the Fengjie County, Th-  
11 ree-Gorge reservoir area, China. *Natural Hazards*, 108, 1-28. <https://doi.org/10.1007/s11069-021-04691-z>.
- 12  
13 Wang, K., Zhang, S., & Wei, F. 2019. Geotechnical mechanical parameters determination of pr-  
14 ediction unit based spatial interpolation technique. *JOURNAL OF NATURAL DISAS-  
15 TERS*, 28, 209-219. <https://doi.org/10.13577/j.jnd.2019.0523>.
- 16 Wang, K., Zhang, S., Xie, W.-l., & Guan, H. 2023. Prediction of the instability probability for  
17 rainfall induced landslides: the effect of morphological differences in geomorphology w-  
18 ithin mapping units. *Journal of Mountain Science*, 20, 1249-1265. <https://doi.org/10.1007/s11629-022-7789-4>.
- 19  
20 Wang, X., Zhang, L., Wang, S., & Lari, S. 2013. Regional landslide susceptibility zoning with  
21 considering the aggregation of landslide points and the weights of factors. *Landslides*,  
22 11. <https://doi.org/10.1007/s10346-013-0392-6>.
- 23 Yan, G., Cheng, H., Jiang, Z., Teng, L., Tang, M., Shi, T., Jiang, Y., Yang, G., & Zhou, Q. 2  
24 021. Recognition of Fluvial Bank Erosion Along the Main Stream of the Yangtze Rive-  
25 r. *Engineering*, 19. <https://doi.org/10.1016/j.eng.2021.03.027>.
- 26 Zhang LY, Zhang JM (2006) Extended algorithm using Monte Carlo techniques for searching g-  
27 eneral critical slip surface in slope stability analysis. *Yantu Gongcheng Xuebao Chin J*  
28 *Geotech Eng* 28(7):857–862 (in Chinese)
- 29 Zhang, S., Ma, Z., Li, Y., Hu, K., Zhang, Q., & Li, L. 2021. A grid-based physical model to  
30 analyze the stability of slope unit. *Geomorphology*, 391, 107887. <https://doi.org/10.1016/j.geomorph.2021.107887>.
- 31  
32 Zhang, S., Xu, C. X., Wei, F., Hu, K., Xu, H., Zhao, L. Q., & Zhang, G. P. 2019. A physics  
33 -based model to derive rainfall intensity-duration threshold for debris flow. *Geomorphol-  
34 ogy*, 351, 106930. <https://doi.org/10.1016/j.geomorph.2019.106930>.
- 35 Zhang, S., Zhao, L., Delgado Tellez, R., & Bao, H. 2018. A physics-based probabilistic foreca-  
36 sting model for rainfall-induced shallow landslides at regional scale. *Natural Hazards a-  
37 nd Earth System Sciences*, 18, 969-982. <https://doi.org/10.5194/nhess-18-969-2018>.
- 38 Zhuang, J., Iqbal, J., Jianbing, P., & Tieming, L. 2014. Probability Prediction Model for Landsl-  
39 ide Occurrences in Xi'an, Shaanxi Province, China. *Journal of Mountain Science*, 11, 3  
40 45-359. <https://doi.org/10.1007/s11629-013-2809-z>.
- 41 Zhuang, J., Peng, J., Xu, Y., Xu, Q., Zhu, X., & Li, W. E. I. 2016. Assessment and mapping  
42 of slope stability based on slope units: A case study in Yan'an, China. *Journal of Eart-  
43 h System Science*, 125. <https://doi.org/10.1007/s12040-016-0741-7>.